Anisotropic lattice softening near the structural phase transition in the thermosalient crystal 1,2,4,5-tetrabromobenzene

Journal Name

ARTICLE

Anisotropic lattice softening near the structural phase transition in the thermosalient crystal 1,2,4,5-tetrabromobenzene

Received 00th January 20xx,
Accepted 00th January 20xx

DOI: 10.1039/x0xx00000x

www.rsc.org/

Boris A. Zakharov,[ab]† Adam A.L. Michalchuk,[bcd] Carole A. Morrison[c] and Elena V. Boldyreva[ab]

The thermosalient effect (crystal jumping on heating) attracts much attention as both an intriguing academic phenomenon, as well as in relation to its potential for the development of molecular actuators. This effect has been documented in many papers. Still, its mechanism remains unclear. 1,2,4,5-Tetrabromobenzene (TBB) is one of the most extensively studied thermosalient compounds that has been shown previously to undergo a phase transition on heating, accompanied by crystal jumping and cracking. The difference in the crystal structures and intermolecular interaction energies of the low- and high-temperature phases is, however, too small to account for the large stress that arises over the course of the transformation. The energy is released spontaneously, and crystals jump across distances that exceed the crystal size by orders of magnitude. In the present work, the anisotropy of lattice strain is followed across the phase transition by single-crystal X-ray diffraction, focusing on the structural evolution from 273 to 343 K. A pronounced lattice softening is observed close to the transition point, with the structure becoming more rigid immediately after the phase transition. The diffraction studies are further supported by theoretical analysis of pairwise intermolecular energies and zone-centre lattice vibrations. Only three modes are found to monotonically soften up to the phase transition, with complex behaviour exhibited by the remaining lattice modes. The thermosalient effect is delayed with respect to the structural transformation itself. This can originate from the martensitic mechanism of the transformation, and the accumulation of stress associated with vibrational switching across the phase transition. The finding of this study sheds more light on the nature of the thermosalient effect in 1,2,4,5-tetrabromobenzene and can be applicable also to other thermosalient compounds.

Introduction

The conversion of energy into motion is a fundamental process in nature. The conversion of photo, thermal or chemical energy into motion by mechanically responsive materials is of particular interest in materials science. Solid-state transformations serve as excellent systems for studying these phenomena, as they are often accompanied by the generation and relaxation of mechanical stress and strain. The terms "thermosalient crystals" [1], or "thermosalient effect" [2] were proposed for crystalline materials that display a mechanical response on heating or cooling. This effect has been documented in many papers, although its mechanism remains disputed. 1,2,4,5-Tetrabromobenzene (TBB) has been one of the most extensively studied "thermosalient crystals" in recent decades. This compound undergoes a first-order phase transition from the *β*- to *γ*-phase on heating, which is accompanied by crystal jumping and/or cracking [3–8]. The crystal structures before and after the phase transition were studied by single-crystal and powder X-ray diffraction [5,9,10] and spectroscopic techniques [11–13], and the acoustic emission across the phase transition was also measured [14]. The thermosalient effect was followed by kinematic analysis [7,8]. Nanoindentation revealed a strong anisotropy in mechanical properties of the low-temperature *β*-phase [7]. Based on these observations the thermosalient phenomenon in TBB was proposed to occur in two stages: (1) accumulation of strain as a result of the phase transition, and (2) sudden release of strain, resulting in ballistic crystal displacement [7]. This release of energy is often accompanied by separation of debris or explosion [7]. Accumulation of the large anisotropic strain on heating prior to the thermosalient phase transition (when a cooperative reorientation of molecules is triggered) was suggested to result from the high elasticity of TBB crystals. The very rapid and nearly instantaneous phase transition itself, was subsequently thought to occur in the selected domains and through the entire crystal. The progression of this structural rearrangement throughout the crystal in a preferred direction is believed to make the crystal move, jumping across

[a] Institute of Solid State Chemistry and Mechanochemistry, Siberian Branch of the Russian Academy of Sciences, Kutateladze Str. 18, Novosibirsk, 630128, Russian Federation
[b] Novosibirsk State University, Pirogova Str. 2, Novosibirsk, 630090, Russian Federation
[c] EaStChem School of Chemistry, University of Edinburgh, Edinburgh, David Brewster Rd, UK, EH9 3FJ
[d] EPSRC Centre for Continuous Manufacturing and Crystallisation (CMAC), UK
† Correspondence email: b.zakharov@yahoo.com

Electronic Supplementary Information (ESI) available: CIFs and structure factor files, CheckCIF report, MS Word file with dependencies of lattice parameters on temperature for all tested crystals, information on Raman modes assignment and calculations.

distances significantly exceeding its own size [7]. Though very attractive, this model does not explain how such small difference in the crystal structures of the low- and high-temperature phases can account for the large mechanical response, where crystals are observed to jump across distances orders of magnitude larger than the crystal size.

Some phase transitions that occur between phases with similar crystal structures and the same crystal symmetry (re-entrant phase transitions, *e.g.* [15]) were shown to occur through an intermediate phase that exists only briefly, in a narrow temperature window of *ca* 10 K. This intermediate phase differs significantly from both the preceding and subsequent phases [16]. One could suppose that a similar situation could exist in TBB. Although the crystal structures of the *β*- and *γ*-phases have been refined at single temperature points before and after the phase transition [7,9,10], the structure has not been monitored at temperatures immediately up to and following the phase transition. This structural data could offer unambiguous determination of anisotropic lattice strain, and the possible existence of any intermediate phases involved in the thermosalient phenomenon of TBB [16,17]. While previous work has reported variable-temperature powder X-ray diffraction data, [5] it was not sufficient to provide this detailed information.

An alternative model was proposed by [13] based on Brillouin light scattering spectroscopy. The lowest transverse acoustic mode exhibited a substantial softening on approaching the phase transition on heating. This was supposed to indicate that the transition is driven by the elastic instability of this soft acoustic mode. While lattice softening may explain the mechanism by which the phase transition itself occurs, it again does not offer a mechanism to the large release of mechanical energy.

The present study aimed to follow the changes in the crystal structure of TBB by single-crystal X-ray diffraction at multiple temperature points. By obtaining these data, we aimed to follow the structural evolution across the phase transition, *i.e.* atomic coordinates and the anisotropy of lattice strain for both the low- and the high-temperature phases, as well as the strain induced by the phase transition itself. With view of better understanding the thermosalient effect, particular focus rests on understanding the associated lattice energies, non-covalent interactions and vibrational structure up to, and through the transition, in relation to the models previously suggested in the literature.

Experimental

Samples and crystallization

1,2,4,5-tetrabromobenzene (Sigma-Aldrich, 97%; 200 mg) was dissolved in chloroform (Baza №1 Khimreaktivov, 98%; 9 mL). Single crystals were grown by slow evaporation at room temperature.

Variable-temperature single-crystal X-ray diffraction

A variable-temperature single-crystal X-ray diffraction study was performed using a *STOE IPDS II* diffractometer with Mo*Kα* radiation and an image-plate detector. An *Oxford Cryostream* cooling device was used to control the sample temperature by N_2 flow (heating rate 50 K/hour). A single crystal of 1,2,4,5-tetrabromobenzene was placed into a 0.2 mm glass capillary (wall thickness 0.01 mm) together with a drop of *NVH* oil (Cargille) ‡ . The sample was heated from 273 to 343 K in 10 K steps across the phase transition point, which was previously reported as *ca* 320 K on heating and *ca* 307 K on reverse cooling [4]. Diffraction data were collected at each temperature point (273, 283, 293, 303, 313, 323, 333, 343 K), in order to refine the crystal structure and calculate the anisotropy of lattice strain. In this series of experiments an 0.8 mm collimator and crystals of dimension 0.72 × 0.11 × 0.03 mm were used. These crystals were slightly larger than generally acceptable crystal sizes, with typical largest linear dimensions of 0.5 mm. In the present case, larger crystals allowed a reduced data collection time without loss of diffraction data quality.

Parameters characterising data collection and crystal structure refinement are summarised in Table 1. *X-AREA* [18] was used for data collection; *CrysAlis Pro* [19] – for data reduction and cell refinement. Crystal structure at all the temperatures was solved with *SHELXS-2016* [20] and refined using *SHELXL-2017* [21] with *ShelXle* as a GUI [22]. Atomic parameters for non-hydrogen atoms were refined in the anisotropic approximation. H-atoms were located in the difference Fourier map and refined using a riding model with $U_{eq}(H) = 1.2\ U_{eq}(C)$. *Platon* [23] and *Mercury* [24] were used for structure validation and visualisation. *Win_Strain* [25] software was used to calculate the anisotropy of lattice strain. Non-incremental strain was calculated in relation to the crystal structure at 273 K, while incremental strain was calculated between the structures corresponding to neighbouring pairs of temperature values, *e.g.* 273-283, 283-293, 293-303 K, *etc.* Complete structural data were deposited in the CSD [26] with refcodes CCDC 1578618-1578625.

Table 1. Parameters characterizing data collection and crystal structure refinement. For all structures: $C_6H_2Br_4$, M_r = 393.72, monoclinic, $P2_1/n$, Z = 2, crystal size (mm) 0.72 × 0.11 × 0.03. Experiments were carried out with Mo $K\alpha$ radiation. Refinement was on 47 parameters. H-atom parameters were constrained.

Crystal data				
Temperature (K)	273	283	293	303
a, b, c (Å)	4.0055 (2), 10.6493 (4), 10.2948 (4)	4.0108 (2), 10.6672 (4), 10.2811 (4)	4.0172 (2), 10.6917 (4), 10.2615 (4)	4.0233 (2), 10.7193 (4), 10.2355 (5)
β (°)	100.172 (4)	100.168 (4)	100.175 (5)	100.184 (5)
V (Å^3)	432.24 (3)	432.96 (3)	433.81 (3)	434.47 (4)
No. of reflections for cell measurement	1774	1749	1634	1637
θ range (°) for cell measurement	4.4–28.2	4.0–28.2	4.0–28.2	4.0–28.2
μ (mm^{-1})	18.54	18.51	18.47	18.45
Data collection				
T_{min}, T_{max}	0.108, 0.574	0.048, 0.549	0.049, 0.551	0.048, 0.575
No. of measured, independent and observed [I > 2σ(I)] reflections	2898, 877, 763	2945, 877, 762	2971, 882, 757	3078, 886, 745
R_{int}	0.035	0.030	0.031	0.022
(sin θ/λ)$_{max}$ (Å^{-1})	0.625	0.625	0.625	0.624
Range of h, k, l	h = -5→4, k = -12→13, l = -12→12	h = -5→4, k = -12→13, l = -12→12	h = -5→4, k = -12→13, l = -12→12	h = -4→5, k = -13→13, l = -12→12
Refinement				
$R[F^2 > 2\sigma(F^2)]$, $wR(F^2)$, S	0.028, 0.074, 1.03	0.030, 0.081, 1.04	0.030, 0.079, 1.03	0.023, 0.052, 1.04
No. of reflections	877	877	882	886
Δρ$_{max}$, Δρ$_{min}$ (e Å^{-3})	0.60, -0.56	0.52, -0.54	0.50, -0.56	0.63, -0.28
Crystal data				
Temperature (K)	313	323	333	343
a, b, c (Å)	4.0549 (3), 11.0780 (5), 9.8719 (5)	4.0618 (3), 11.1039 (5), 9.8533 (5)	4.0686 (3), 11.1298 (5), 9.8431 (5)	4.0723 (3), 11.1474 (6), 9.8296 (6)
β (°)	100.585 (5)	100.618 (5)	100.640 (6)	100.671 (7)
V (Å^3)	435.90 (4)	436.79 (4)	438.06 (4)	438.50 (5)
No. of reflections for cell measurement	1482	1477	1547	1481
θ range (°) for cell measurement	4.2–28.2	2.8–28.2	2.8–28.2	2.8–28.2
μ (mm^{-1})	18.39	18.35	18.30	18.28
Data collection				
T_{min}, T_{max}	0.046, 0.561	0.045, 0.579	0.050, 0.563	0.048, 0.581
No. of measured, independent and observed [I > 2σ(I)] reflections	3020, 891, 725	3093, 892, 721	3048, 895, 696	3134, 893, 666
R_{int}	0.033	0.026	0.038	0.035
(sin θ/λ)$_{max}$ (Å^{-1})	0.625	0.625	0.625	0.625
Range of h, k, l	h = -5→4, k = -13→13, l = -12→12	h = -4→5, k = -13→13, l = -12→12	h = -5→4, k = -13→13, l = -12→12	h = -4→5, k = -13→13, l = -12→12
Refinement				
$R[F^2 > 2\sigma(F^2)]$, $wR(F^2)$, S	0.033, 0.088, 1.04	0.028, 0.067, 1.07	0.039, 0.100, 1.03	0.032, 0.073, 1.05
No. of reflections	891	892	895	893
Δρ$_{max}$, Δρ$_{min}$ (e Å^{-3})	0.67, -0.43	0.56, -0.44	0.78, -0.59	0.58, -0.45

Raman spectroscopy

A single-crystal Raman spectrum was collected at ambient temperature using a LabRAM HR 800 Raman spectrometer from HORIBA Jobin Yvon, with a CCD detector. The 488 nm line of an Ar^+ laser was used for spectral excitation with beam diameter *ca* 1 μm. The laser power was approximately 8 mW. The spectrum was measured in 180º backscattering collection geometry with a Raman microscope.

Computational methods

Input unit cells were taken from experimentally determined X-ray diffraction structures, as determined above. All calculations were performed using the generalised gradient DFT functional of Perdew-Burke-Ernzerhof, PBE [27] with the Grimme D3 dispersion correction [28]. Norm-conserving pseudopotentials were used throughout. The wavefunction was sampled on a Monkhorst-Pack (MP) grid [29], with reciprocal space k-spacing of no more than 0.05 Å^{-1}. A plane-wave kinetic energy cut-off of 1800 eV was used. To ensure calculations pertain to the correct geometry, and ensuring minimal computational bias, unit cell parameters were held fixed to the experimental values. The ionic positions were allowed to relax until the force on each atom fell below 10^{-4} eV and the total change in energy was converged to 10^{-9} eV. The wavefunction convergence was set to 10^{-10} eV to ensure accurate calculation of the Hellman-Feynman forces. Phonon calculations were performed using Density Functional Perturbation Theory (DFPT), as implemented in CASTEP v17.2 [30,31]. Zone-centre (Γ-point) vibrations were calculated for the optimised unit cells for comparison with experimental Raman frequencies. The acoustic sum rule was applied in reciprocal space.

The optimised geometry was extracted from the above calculation, and used as input for single point calculations in Quantum Espresso v5.4 [32]. All atoms were treated using PAW pseudopotentials, with energy cut-off for the wave function of 133 Ry (1809 eV). The same DFT functional and reciprocal space k-point grid were used as above. Non-covalent interaction maps were generated using the resulting electron density with the NCIplot code [33,34], as implemented in Critic2 [35], and Crystal Orbital Hamilton Population analysis performed using Lobster v2.0. [36–39]. Symmetry Adapted Perturbation Theory (SAPT) calculations were performed using jun-cc-pVDZ

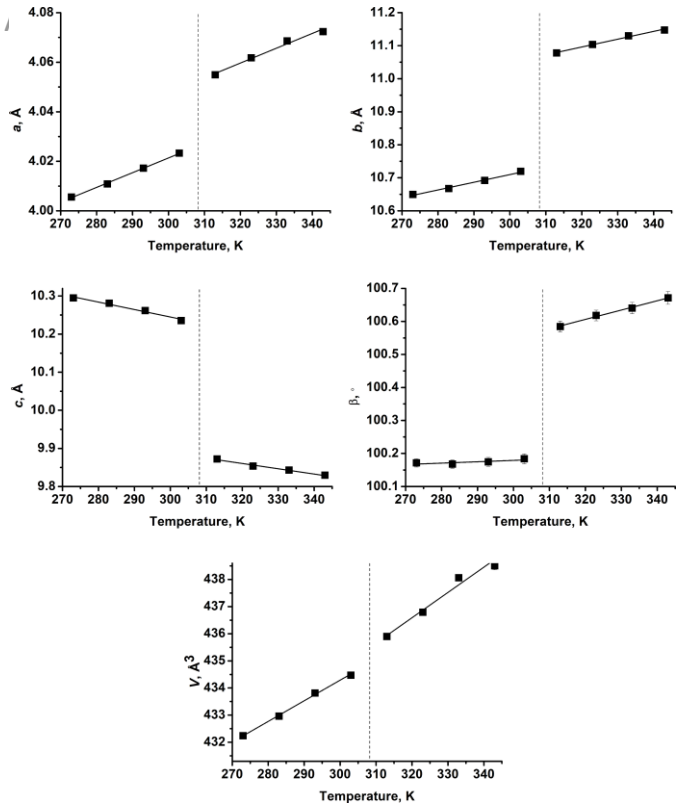

Figure 1. The lattice parameters of 1,2,4,5-tetrabromobenzene *vs*. temperature

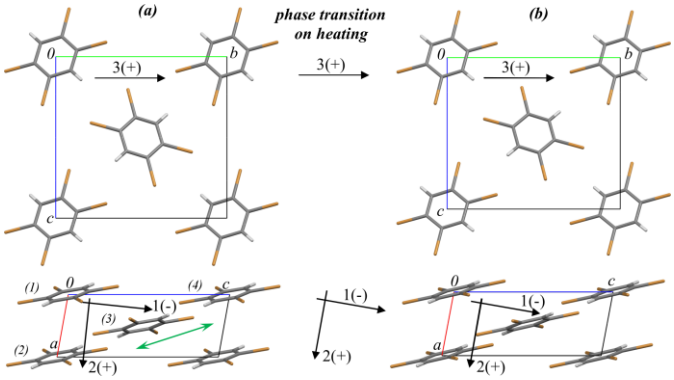

Figure 2. The fragments of crystal structures of 1,2,4,5-tetrabromobenzene (TBB) before (303 K, a) and after (313 K, b) the phase transition from *β*- to *γ*-phase. Arrows show directions of principal axes of strain ellipsoid before, during and after the phase transition on heating. (+) and (-) signs indicate positive and negative deformations on heating correspondingly. Green double arrow shows the direction of the relative shift of the TBB layers during the phase transition

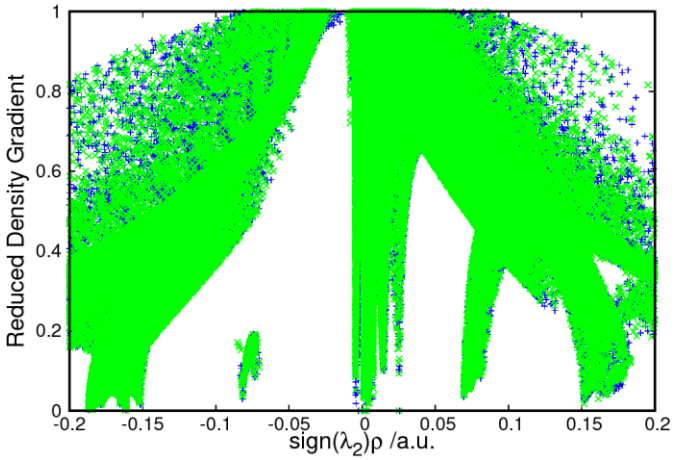

Figure 3. Non-covalent interaction (NCI) map for the TBB polymorphs. The 2-dimensional integration of NCI maps for *β*-TBB (green) and *γ*-TBB (blue)

basis sets for each atom using the sSAPT0 [40,41], the bronze standard SAPT method [42]. SAPT calculations were performed using Psi4 v 1.1 [43].

Results and discussion

A structural phase transition from the *β*- to *γ*-phase was observed (Figure 1) at slightly lower temperatures (between 303 and 313 K) as compared to some previously reported values (316-321 K) [4,5,7,8], agreeing well with the transition temperature of 307 K reported elsewhere [3]. This discrepancy is likely related to different quantities of impurities in the samples, including defects, which can shift the phase transition temperature by several degrees. Further factors may include differences in the heating protocol (heating rate) and uncertainties associated with temperature measurement across various works. No intermediate phase could be detected with data collection times of *ca* 15 hours. Should any such phase exist, its lifetime must be well below this limit. Previous spectroscopic measurements also did not reveal any intermediate phase on the order of minutes with faster overall heating through the phase transition [13].

The crystal structures of the two polymorphs before and after the phase transition agree well with literature data (Figure 2). In the present contribution we used cell setting with $P2_1/n$ space group symmetry. From initial observation, the changes in the molecular packing associated with this transition appear only minute. Indeed, analysis of the non-covalent interaction (NCI) maps by means of the reduced density gradient [34] suggests that the non-covalent interactions contained within the TBB lattice in both polymorphs remain nearly identical, and thus only minimal changes in the intermolecular contacts occur across the phase transition, Figure 3. Structurally, one would therefore not expect the drastic mechanical response across the *β*- to *γ*- phase transition that has been observed previously. The volume change corresponding to the phase transition was 0.3 % (on heating from 303 to 313 K). This value is more typical for phase transitions that are not accompanied by a noticeable mechanical response. For transformations accompanied by

Table 2. Principal linear strain values and the orientations of principal axes of strain ellipsoid in relation to cell vectors on heating. All values calculated in relation to 273 K, 303 K and 313 K for heating of the *β*-phase, for the phase transition from *β*- to *γ*-phase on heating and for heating of the *γ*-phase, respectively

273 → 303 K, LT *β*-phase			Angles to (º)		
Principal strain		ESD	*a*	*b*	*C*
Axis 1	-0.005881	0.000060	94.5(0.4)	90.0(0.0)	5.7(0.4)
Axis 2	0.004479	0.000079	175.5(0.4)	90.0(0.0)	84.3(0.4)
Axis 3	0.006546	0.000054	90.0(0.0)	180.0(0.0)	90.0(0.0)
303 → 313 K, *β*-*γ* phase transition			Angles to (º)		
Principal strain		ESD	*a*	*b*	*C*
Axis 1	-0.037384	0.000068	91.1(0.1)	90.0(0.0)	9.5(0.1)
Axis 2	0.007898	0.000089	1.1(0.1)	90.0(0.0)	99.5(0.1)
Axis 3	0.032907	0.000059	90.0(0.0)	0.0(0.0)	90.0(0.0)
313 → 343 K, HT *γ*-phase			Angles to (º)		
Principal strain		ESD	*a*	*b*	*C*
Axis 1	-0.004578	0.000079	90.4(0.5)	90.0(0.0)	10.3(0.5)
Axis 2	0.004285	0.000100	179.6(0.5)	90.0(0.0)	79.7(0.5)
Axis 3	0.006248	0.000066	90.0(0.0)	180.0(0.0)	90.0(0.0)

thermosalient and photosalient effects, the typical values of volume change are usually several percent ([8] and refs therein), and can reach over 10 % ([2] and refs therein).

In cases of relatively small structural changes, the origin of large mechanical effects can be sought in the anisotropy of strain [2,7,44–46]. In fact, strain accompanying the phase transition in TBB is strongly anisotropic (Table 2, Figure 2). The directions of the principal axes of the strain ellipsoids in both the low-temperature *β*- and the high-temperature *γ*-phases are very close to each other. Across the entire temperature range, the direction of the largest *positive* thermal expansion (principal axis 3) is along the crystallographic *b*-axis. It corresponds to deformation of the TBB flat layers, which are parallel to (101). The rotation of axes 1 and 2 of the strain ellipsoid does not exceed 5º. The direction of principal axis 1 corresponds to the largest *negative* thermal expansion; it is close to the crystallographic *c*-axis. The negative thermal expansion along axis 1 together with the positive thermal expansion along axis 2 result in a shift of the TBB layers parallel to (101) in the [-101] direction (Figure 2).

While the orientations of the principal axes of the strain ellipsoid across the phase transition are almost the same, the strain values are different (Figure 4). The structure first becomes softer on heating (the incremental strain values increase), in agreement with Brillouin spectroscopic results [13],

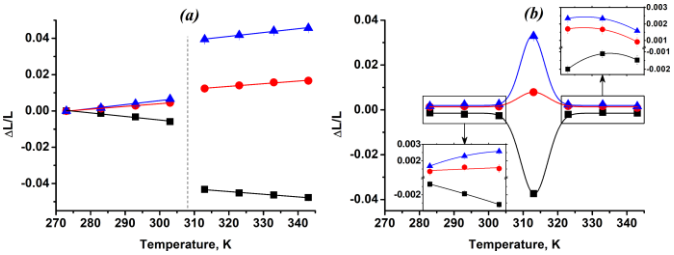

Figure 4. Non-incremental (a) and incremental (b) finite Eulerian strain for 1,2,4,5-tetrabromobenzene. Principal axes of strain ellipsoid 1, 2 and 3 are shown as squares, circles and triangles correspondingly

followed by the expected phase transition. This transition is accompanied by significant deformations, and becomes more rigid with increasing temperature after the phase transition. The crystal structures of both the *β*- and *γ*-phases are softest at temperatures close to the phase transition point. The absolute strain values at the moment of the phase transition on heating from 303 to 313 K are approximately 14 times higher in the direction of principal axis 1, approximately 5 times higher in the direction of principal axis 2, and approximately 13 times higher in the direction of principal axis 3, as compared to the corresponding strain values achieved on heating from 293 to 303 K before the phase transition (Figure 4). In order to achieve the same values of structural strain without the phase transition, it would be necessary to heat the crystal to 370-420 K. Such anisotropic strain accompanying a phase transition is typical for thermosalient materials [2,7,44–46].

While it has been noted previously that the *β*-*γ* transition is endothermic, it remains interesting to examine the pairwise intermolecular energies as a function of temperature. In particular, to identify whether stabilisation of select interactions may be responsible for the initiation of the phase transition. Analysis of intermolecular interactions were performed on three TBB dimers, extracted from the unit cell, namely between molecules 1-2, 2-3 and 3-4, Figure 2. These dimers were selected so as to represent the major intermolecular interactions, the π-π stacking interaction, dimer 1-2, and the two potential halogen bonding interactions, dimers 2-3 and 3-4.

The total stabilising energy of dimer 1-2 at 273 K is -33.01 KJ.mol^{-1}, similar to related interaction strengths in other substituted aromatics [47]. Energy decomposition of the π-π stacking interaction in the 273 K structure reveals the expected dispersion stabilisation, with a dispersion energy of -59.27 KJ.mol^{-1}. The electrostatic contribution is also large, having an energy of -16.18 KJ.mol^{-1}. There is a large destabilising exchange contribution, 45.38 KJ.mol^{-1}, with only negligible inductive stabilisation, -2.94 KJ.mol^{-1}. As the temperature is increased, the magnitude of each component of the interactions decreases with thermal expansion, ESI. However, the total energy is found to initially destabilise (by *ca* 0.31 KJ.mol^{-1}), restabilising on further heating, such that the total energy at 303 K is approximately equal to that of the 273 K structure. This initial discontinuity is reflected in structural parameters of intermolecular contacts (ESI). Despite the negligible atomic displacement associated with the phase

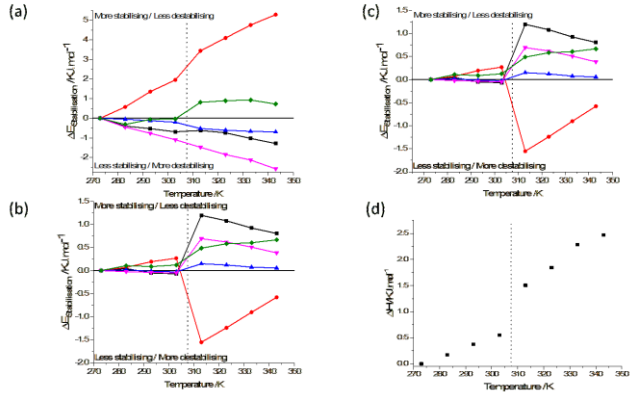

Figure 5. Stabilisation energies for TBB as a function of temperature. SAPT energy decomposition for (a) dimer 1-2, (b) dimer 2-3 and (c) dimer 3-4. The relative stabilising contribution is shown for (red) exchange, (blue) induction, (black) electrostatic, (pink) dispersion and (green) total energy. A dotted line identifies the phase transition temperature. (d) The change in lattice enthalpy as a function of temperature

transition, there is an obvious discontinuity in the pair-wise stabilisation energies across the phase transition, Figure 5. From 303 K to 313 K, there is a particularly notable decrease in the exchange (destabilising) contribution. This leads to an overall increase in stabilisation of the π-π stacking interaction by 0.84 KJ.mol^{-1}. On further heating after the phase transition, the energy of the π-π stacking interaction remains approximately constant, with signs of its weakening at higher temperatures as the crystallographic *a*-axis continues to expand.

The absolute energy of dimers 2-3 and 3-4 is lower than that of 1-2, Tables S1-S3, with a stabilisation energy of only -12.94 KJ.mol^{-1} at 273 K. We note that there is once again a discontinuity in the change in energy at 283 K. The energy first stabilises by *ca* 0.1 KJ.mol^{-1}, destabilises slightly, then again stabilising by a further 0.04 KJ.mol^{-1}. This apparent optimisation of intermolecular interactions of both the 1-2, and 2-3/3-4 dimers towards the phase transition may suggest a partial mechanism for the observed structural softening. Pairwise intermolecular stabilisation thereby reducing energy penalties induced by strain. The phase transition is signified by a notable discontinuity in the dimer interaction energy, with an increased stabilisation of 0.36 KJ.mol^{-1}. As compared with dimer 1-2, however, all energy components contribute to this effect, Figures 5. With four such interactions in the unit cell, a total stabilisation of approximately 1.46 KJ.mol^{-1} is expected from these interactions across the phase transition.

Based on pairwise intermolecular interactions, a total stabilisation of approximately 2.31 KJ.mol^{-1} occurs as a result of the phase transition. This energy alone is often sufficient to describe the energy difference between polymorphic forms of molecular materials.

Similar to hydrogen bonds, halogen-bonding interactions are often thought to contain some charge transfer character. This is often the case observed in orthogonally interacting halogen atoms, as is the case in TBB. Any potential increase in covalency across the phase transition would immediately suggest a driving force to the phase transition. While the decomposition of interacting energies by SAPT does not suggest strong charge transfer character across any of the studied structures, SAPT does not allow isolation of Br…Br or H…Br interactions. To identify any potential covalency in these interactions, the projected Crystal Orbital Hamilton Population (COHP) is studied. This method projects the electronic density of states, weighted by the associated interaction Hamiltonian element. Thus, an integration of the pCOHP up to the Fermi level offers an indication of the covalent bond energy. In the present case, it is seen that the total integrated pCOHPs for all Br…Br and H…Br interactions present in the crystal fall within a magnitude < 0.1 eV [48]. This is strongly supportive of the fact that no covalent character is present within the Br…Br or H…Br interactions, and that all intermolecular interactions are purely non-covalent in nature.

According to the above analysis, the phase transition is associated with an increased stabilisation of the three pair-wise intermolecular interactions. In contrast, however, the calculated enthalpies for each experimental crystal structure suggests that the overall enthalpic trend is destabilising, Figure 5. One observes an increase in the enthalpy by 0.95 KJ.mol^{-1}, a value similar to previous experimental reports [3]. This discrepancy between pairwise interaction energies and lattice enthalpies has been noted previously [49]. Thus, while individual pairwise interactions may be optimised across the transition, the overall molecular packing does not reflect this. Regardless, it is clear from this work that the release of energy suitable for the observed mechanical response in TBB is not due to an overall enthalpic stabilisation, despite the notable gain in pairwise intermolecular interactions. The mechanical response must therefore be associated with an entropic effect, associated with the vibrational structure of the material.

It is particularly interesting to find that this lattice softening is not obvious from analysis of the lattice enthalpy, although some indication may be observed in analysis of the pairwise intermolecular interactions. Thus, it was prudent to follow the change in the zone-centre vibrational structure on increasing temperature. Both phases of TBB adopt monoclinic space group $P2_1/n$, with zone-centre point group C_{2h} (2/m). One expects a total of 72 vibrations ($18A_g$, $18A_u$, $18B_g$ and $18\ B_u$), of which 12 are external modes ($\Gamma_{acoustic} = A_u + 2B_u$). One therefore expects nine external optical modes.

To ensure accurate description of our model, calculated Raman frequencies were compared to experimental data [50], for frequencies below 1000 cm^{-1} (Table S5). Excellent agreement is found for all low frequency modes, with slightly larger deviations observed (remaining < 20 cm^{-1}) as frequency increases, as expected. A complete list of calculated frequencies is given in the ESI.

The zone-centre harmonic frequencies calculated for the *β*-TBB structure up to the phase transition suggest that only minor changes occur in the vibrational structure. On heating, the majority of vibrational modes are found to harden, typically by no more than half a wavenumber (ESI). More notably, however is the A_u mode at *ca* 32 cm^{-1} that corresponds to the out of phase translation of neighbouring π-stacked columns of TBB molecules along the crystallographic

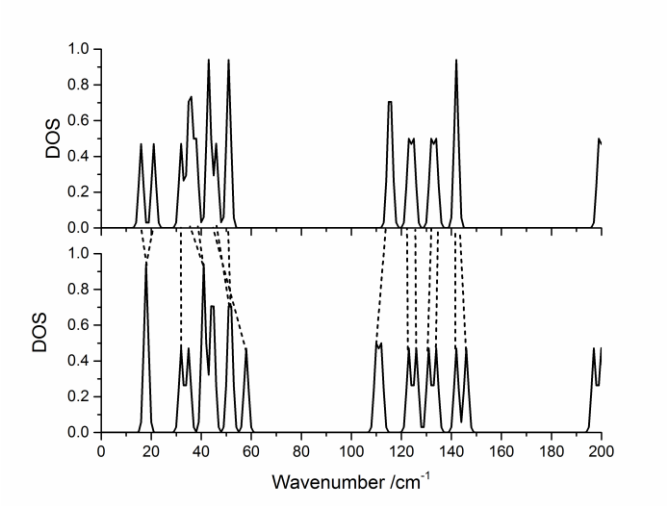

Figure 6. Mapping of vibrational structure between the (bottom) *β*- and (top) *γ*-polymorphs. Dotted lines connected conserved vibrational modes

a-axis. This mode hardens by more than 2 cm^{-1} (6%) over 30 K. This is consistent with pairwise intermolecular energy calculations, which suggest that the bond strength, and thus intermolecular force constant, increases between stacks of molecules. This can be associated to the reduction in the crystallographic *c*-axis on heating. Similarly large hardening is observed for higher frequency modes in the range of 200-300 cm^{-1}, which also correspond to large, concerted motion within π-stacked columns of the TBB molecules along the crystallographic *a*-axis. Again, vibrational hardening can be associated to the perpendicular compression of the *c*-axis.

It is interesting to find that many of the vibrational modes do not harden monotonically. There is a consistent initial softening between 273 and 283 K, as observed by pairwise intermolecular interactions, often with continued softening up to 293 K. Many modes subsequently harden between 293 and 303 K (ESI). Sudden mode hardening is particularly true for eigenvectors with a large component along principal strain axis 3, which begins to harden at this temperature, Figure 4. This behaviour is likely associated with the non-linearity in the strain parameters observed by diffraction (ESI).

Only three low frequency vibrational modes are found to soften monotonically up to the phase transition: (1) the B_g (43.29 cm^{-1}, T = 273 K) mode corresponding to the external rocking motion of the TBB molecules along the crystallographic *a*-axis, (2) the B_g (47.05 cm^{-1}, T = 273 K) mode corresponding to the external rocking of the TBB molecule along the crystallographic *b*-axis, and (3) the B_u mode (61.12 cm^{-1}, T = 273 K) corresponding to a libration mode, composed of Br wag and TBB translation along the crystallographic *b*-axis (ESI). We note that a combination of modes (1) and (2) seem to map the TBB molecule between *β*- and *γ*-TBB.

Despite the minimal structural changes associated with the *β* to *γ* phase transition, the low frequency vibrational structure appears to change quite remarkably, Figure 6. There is a noticeable splitting of the lowest frequency band (*ca* 20 cm^{-1}) across the phase transition. Analysis of the eigenvectors shows that the splitting involves the same normal modes across the phase transition, namely an A_g and a B_g external rocking motion in both cases. In the latter, rocking occurs about the (011) plane, with the A_g rocking axis also along the crystallographic *a*-axis, offset by *ca* 30°. Perhaps the most striking difference between the *β*- and *γ*-polymorph vibrational spectra is the loss of the B_u band at 58.8 cm^{-1} (T = 303 K) across the transition. We note that this mode is soft mode (3) discussed above. Analysis of the eigenvectors suggests that this mode maps onto the B_u mode at 43.8 cm^{-1} (T = 313 K) in the *γ*-phase. We note, however, that the relative magnitude of the Br wag component of the B_u normal coordinate in the *γ*-polymorph is slightly less than in the *β*-form. There is a net atomic displacement resulting from this motion in the *β*-polymorph unit cell, which is parallel to the [011] vector. This is thus perpendicular to the propulsion vector defined previously [7]. The primary motion of this normal coordinate is translation along the crystallographic *b*-axis, with perpendicular Br wag. The rows of TBB molecules aligned perpendicular to the *b*-axis (parallel to *c*), translate out of phase. Thus, it is sensible that larger thermal atomic displacement of this mode should favour expansion in this direction (the third principal strain vector, and largest *positive* thermal expansion).

The second softened mode, mode (2) above, occurs at 41.7 cm^{-1} at 303 K in the *β*-polymorph. This mode can be found to map onto a B_g mode at 35.8 cm^{-1} (T = 313 K) in the *γ*-polymorph. While there is no net displacement of the unit cell as a function of the B_g mode, the atomic motion is analogous to a seesaw. Two planes of molecules are present, with alternating layers oscillating about an axis parallel to (or perpendicular to) the [011]. Thus, these alternating layers lead to net thrust both perpendicular and parallel to the proposed propulsion axis. We note that this normal coordinate is fully in phase along the crystallographic *c*-axis, and it is therefore logical that mode softening should occur with expansion of the *a*- and *b*-axes.

The third softened mode, mode (1) above, is found at 45.16 cm^{-1} in the *β*-polymorph at 303 K. This mode is fully in phase along the crystallographic *c*-axis, with the major repulsive interaction occurring between colliding Br…Br contacts on neighbouring molecules, which rotate out of phase. No net motion of the unit cell accompanies this mode, with each π-stacked column rotating about its own axis, effectively parallel to the crystallographic *a*-axis. Unlike the above modes, this softened mode does not map directly to the *γ*-polymorph, although it is similar to the *γ*-phase B_g mode at 43.30 cm^{-1}. Interestingly, the A_u mode discussed above does not soften across the phase transition, hardening further from 32.12 cm^{-1} at 303 K to 32.67 cm^{-1} at 313 K.

In the higher frequency region of the vibrational structure, no notable changes are observed, except for merging of the two sets of bands at *ca* 1280 cm^{-1}. These four modes correspond to deformation of the TBB aromatic ring. The internal vibrational modes at 110.56 and 112.36 cm^{-1} in the 303 K β-form corresponds to the Au mode in which the benzene rings translate along the π-stacked columns with neighbours out of

phase or in phase, respectively. These modes are maintained and harden across the phase transition, Figure 6. All further modes up to 200 cm^{-1} are fully conserved across the phase transitions, with only minor shifts in frequency. Thus, of all the low frequency modes, only three are unique to either phase.

On continued heating following the phase transition, nearly all modes are found to soften monotonically. This softening occurs to much greater extent for nearly all *γ*-TBB modes (typically 1-4 cm^{-1}) than for any single *β*-TBB mode, across the same magnitude of temperature change (ESI). This highlights the notably different responses of the two TBB polymorphs to heating, and further highlights the complexities that occur within the *β*-phase lattice up to the phase transition.

This sudden and large drop in the lattice mode frequencies can be expected to be associated with an increase in the vibrational entropy of the materials. Based on the zone-centre density of states alone, this is approximately 5 $J.mol^{-1}K^{-1}$ at 300 K, and approximately 15 $J.mol^{-1}.K^{-1}$ across the phase transition. Assuming a linear extrapolation of the enthalpy of the *β*-polymorph to 313 K, this offers approximate 1 $KJ.mol^{-1}$ stabilisation of the *γ*-polymorph over the *β*-form at this temperature. The entropic contribution can be expected to become larger with consideration of a larger portion of the Brillouin zone [51].

Of the 11 optical modes < 100 cm^{-1}, 8 map directly to the *γ*-polymorph, Table S7, with the three remaining modes displaying a shift in their principal polarisation. Interestingly, the major polarisation of the eigenvector associated with the *β*-polymorph Au mode (44.06 cm^{-1}, T = 303 K) shifts from nearly perpendicular to nearly parallel to the principal strain axis across the transition, hardening by *ca* 2 cm^{-1}, Figure S9. While the same is true for the B_g mode, the opposite is true of the A_g mode, Figure S9. On heating, these modes all soften (Figures S4 and S5).

This reorientation of the phonon polarisation axes is particularly interesting given the observation of a delay in the thermosalient effect in TBB ESI. This delay has also been reported previously[7]. The thermosalient effect is not observed until after the structural phase transformation has been observed by single-crystal X-ray diffraction, which suggests a delay in response time on the order of 15 hours (i.e. the time for data collection). As the phase transition is martensitic in nature, such an effect can be expected should domains of each phase coexist near the transition temperature. This coexistence is particularly likely given the small energy gain associated with the phase transition.

The co-existence of β- and γ-TBB domains near the phase transition point is accompanied by phase boundaries. Any phase boundary is accompanied by stress. In the present system, the stress associated with this phase boundary may not be expected to be too large as a result of structural differences alone. However, this particular phase boundary can now be said to be associated with a select set of perpendicularly polarised lattice modes, introducing a dynamic stress to this boundary as phonons propagate towards the phase boundary. The associated stress becomes particularly large if heating is continued. This suggests that these lattice modes are responsible for considerable stress within the newly formed γ-TBB phase, particularly as they are associated with drastic compression along the principal strain axis across the phase transition. One could therefore suggest that the thermosalient effect occurs as follows: (1) Softening of the TA-II mode [13] offers a mechanism to the martensitic phase transition itself, (2) this phase transition occurs only in some domains initially, leading to formation of highly stressed domain boundaries, (3) rapid release of this stress in a concerted manner (leading to completion of the phase transition) results in a large mechanical response. Thus, the thermosalient effect is not a direct result of the transition itself, but a byproduct of it.

The strain of the TBB structure on phase transition from *β*- to *γ*-phase in the direction of the principal axis 2 of strain ellipsoid is low (close to zero) as compared to the strain along the axes 1 and 3, along which the phonon repolarisation occurs. The values of the latter have much higher comparable absolute values, but the opposite signs. This fact agrees with the martensitic nature of the phase transition. The situation, when the growth of a new phase (in the case of the present study the *γ*-form) stops due to the stresses arising at the interface between the parent (*β*-) and product phase (*γ*-) is typical for a martensitic transformation [52]. Therefore, one of the explanations of the delay of the mechanical response with respect to the structural transformation is that the transformation, that looks like a complete when studied by single-crystal X-ray diffraction, has in fact left some inclusions of the parent *β*-phase non-transformed.

Taking into account the strong similarity of the *β*- and *γ*-phases, the *β*-phase may be undetectable by single-crystal X-ray diffraction, if it is preserved only as remaining inclusions in the crystal that has already transformed into the product *γ*-phase, In this case the transformation from the highly stressed metastable state into a pure *γ*-phase can be completed later (at higher temperatures, or if the crystal is kept longer at the same temperature). A strong mechanical response is then caused by the simultaneous release of energy accumulated at the interfaces between the inclusions of the *β*- phase in the *γ*-phase.

The hypothesis that the thermosalient effect can be related to the formation of a poly-domain structure containing both the parent *β*- and the product *γ*-phases has been discussed earlier [8]. It can be indirectly supported by the fact that the thermosalient effect becomes smaller and practically disappears on cycling heating and reverse cooling, when a crystal goes many times through the *β*- to *γ*-form transition and back [8].

Lattice softening observed in TA-II mode by Brillouin spectroscopy [13] is responsible for phase transition, but this accumulation of stress and its sudden release, responsible for mechanical response.

Conclusions

The present study of a thermosalient material, TBB, combining variable-temperature single-crystal X-ray diffraction study and

lattice dynamics calculations has revealed lattice softening at temperatures close to the phase transition point from *β*- to *γ*-phase that accompanies the anisotropic structural strain. The structure of the high-temperature phase becomes more rigid on further heating. This phenomenon can account for the large thermosalient effect that is observed despite a large structural similarity of the low- and high- temperature polymorphs and a small volume change across the phase transition. The delay in the thermosalient effect with respect to the structural transformation itself can originate from the martensitic mechanism of the transformation and be related to the poly-domain structure of the sample. The finding of this study shed more light on the nature of the thermosalient effect in TBB and can be applicable also to other thermosalient compounds.

Conflicts of interest

There are no conflicts to declare.

Acknowledgements

The work was supported by a grant from RFBR (BAZ, research project No. 16-33-60093 mol_a_dk). Further support was given by an Edinburgh Global Research Scholarship (AALM), EPSRC CMAC 1/I033459/1 (AALM) and the Russian Ministry of Science and Education (AALM). The UKCP Consortium and Edinburgh Compute and Data Facility (ECDF) are gratefully acknowledged for access to computational resources. We are grateful to the UK Materials and Molecular Modelling Hub for computational resources, which is partially funded by EPSRC (EP/P020194/1) The authors acknowledge helpful discussions with Dr. S. Chizhik, Dr. A. Matvienko and Prof. Dr. A. Sidelnikov.

Notes and references

‡ Two additional crystals were fixed by NVH oil (Cargille) onto a micro-mesh polymer sample holder from MiTeGen and tested at variable temperatures. This was not sufficient, to avoid crystal jumping away from the sample holder on heating when the temperature of the phase transition was near the phase transition point. The first crystal was lost on heating to 313 K, the second – to 323 K. Structural data for these crystals were refined at 273, 283, 293 and 303 K, and for the first, and at 273, 283, 293, 303 and 313 K for the second crystal , respectively. Both crystals were fixed to holder by (1-10) face since this can influence the observed mechanical response of the crystal [7]. See more details in ESI.

1 J. Gigg, R. Gigg, S. Payne and R. Conant. J. Chem. Soc., Perkin Trans. 1, 1987, 2411–2414.
2 P. Naumov, S. Chizhik, M. K. Panda, N. K. Nath and E. Boldyreva, Chem. Rev., 2015, **115**, 12440–12490.
3 D. Mondieig, M. A. Cuevas-Diarte and Y. Haget, J. Therm. Anal., 1989, **35**, 2491–2500.
4 F. B. Johnson, Nature, 1956, **178**, 590–590.
5 H. F. Lieberman, R. J. Davey and D. M. T. Newsham, Chem. Mater., 2000, **12**, 490–494.
6 K. Schaum, K. Schaeling and F. Klausing, 1916, **411**, 161–195.
7 S. C. Sahoo, S. B. Sinha, M. S. R. N. Kiran, U. Ramamurty, A. F. Dericioglu, C. M. Reddy and P. Naumov, J. Am. Chem. Soc., 2013, **135**, 13843–13850.
8 S. C. Sahoo, M. K. Panda, N. K. Nath and P. Naumov, J. Am. Chem. Soc., 2013, **135**, 12241–12251.
9 G. Gafner, Acta Crystallogr., 1964, **17**, 982–985.
10 G. Gafner, Acta Crystallogr., 1960, **13**, 706–716.
11 K. M. White and C. J. Eckhardt, J. Chem. Phys., 1989, **90**, 4709–4718.
12 R. C. Dye and C. J. Eckhardt, J. Chem. Phys., 1989, **91**, 3624–3630.
13 J.-H. Ko, K.-S. Lee, S. Chandra Sahoo and P. Naumov, Solid State Commun., 2013, **173**, 46–50.
14 M. K. Panda, M. Etter, R. E. Dinnebier and P. Naumov, Angew. Chemie Int. Ed., 2017, **56**, 8104–8109.
15 C. Brinkmann, H. Eckert, D. Wilmer, M. Vogel, J. S. auf der Günne, W. Hoffbauer, F. Rau and A. Pfitzner, Solid State Sci., 2004, **6**, 1077–1088.
16 D. Chernyshov, M. Hostettler, K. W. Törnroos and H.-B. Bürgi, Angew. Chemie Int. Ed., 2003, **42**, 3825–3830.
17 A. A. Matvienko, D. V. Maslennikov, B. A. Zakharov, A. A. Sidelnikov, S. A. Chizhik and E. V. Boldyreva, IUCrJ, 2017, **4**, 588–597.
18 X-AREA. STOE&CIE, 2013.
19 RigCrysAlisPro. Rigaku-Oxford Diffraction, 2016.
20 G. M. Sheldrick, Acta Crystallogr. A., 2008, **64**, 112–122.
21 G. M. Sheldrick, Acta Crystallogr. C., 2015, **71**, 3–8.
22 C. B. Hübschle, G. M. Sheldrick and B. Dittrich, J. Appl. Crystallogr., 2011, **44**, 1281–1284.
23 A. L. Spek, Structure validation in chemical crystallography., Acta Crystallogr. D. Biol. Crystallogr., 2009, **65**, 148–155.
24 C. F. Macrae, P. R. Edgington, P. McCabe, E. Pidcock, G. P. Shields, R. Taylor, M. Towler and J. van de Streek, J. Appl. Crystallogr., 2006, **39**, 453–457.
25 R. J. Angel, Win_Strain, 2011, www.rossangel.com.
26 F. H. Allen, Acta Crystallogr. B., 2002, **58**, 380–388.
27 J. P. Perdew, K. Burke and M. Ernzerhof, Phys. Rev. Lett., 1996, **77**, 3865–3868.
28 S. Grimme, J. Comput. Chem., 2006, **27**, 1787–1799.
29 H. J. Monkhorst and J. D. Pack, Phys. Rev. B, 1976, **13**, 5188–5192.
30 K. Refson, P. R. Tulip and S. J. Clark, Phys. Rev. B, 2006, **73**, 155114.
31 S. J. Clark, M. D. Segall, C. J. Pickard, P. J. Hasnip, M. I. J. Probert, K. Refson and M. C. Payne, Z. Krist., 2005, **220**, 567–570.
32 P. Giannozzi, S. Baroni, N. Bonini, M. Calandra, R. Car, C. Cavazzoni, D. Ceresoli, G. L. Chiarotti, M. Cococcioni, I. Dabo, A. Dal Corso, S. de Gironcoli, S. Fabris, G. Fratesi, R. Gebauer, U. Gerstmann, C. Gougoussis, A. Kokalj, M. Lazzeri, L. Martin-Samos, N. Marzari, F. Mauri, R. Mazzarello, S. Paolini, A. Pasquarello, L. Paulatto, C. Sbraccia, S. Scandolo, G. Sclauzero, A. P. Seitsonen, A. Smogunov, P. Umari and R. M. Wentzcovitch, J. Phys. Condens. Matter, 2009, **21**, 395502.
33 J. Contreras-García, E. R. Johnson, S. Keinan, R. Chaudret, J.-P. Piquemal, D. N. Beratan and W. Yang, J. Chem. Theory Comput., 2011, **7**, 625–632.
34 E. R. Johnson, S. Keinan, P. Mori-Sánchez, J. Contreras-García, A. J. Cohen and W. Yang, J. Am. Chem. Soc., 2010, **132**, 6498–6506.
35 A. Otero-de-la-Roza, E. R. Johnson and V. Luaña, Comput. Phys. Commun., 2014, **185**, 1007–1018.
36 R. Dronskowski and P. E. Bloechl, J. Phys. Chem., 1993, **97**, 8617–8624.
37 V. L. Deringer, A. L. Tchougréeff and R. Dronskowski, J. Phys. Chem. A, 2011, **115**, 5461–5466.
38 S. Maintz, V. L. Deringer, A. L. Tchougréeff and R. Dronskowski, J. Comput. Chem., 2013, **34**, 2557–2567.
39 S. Maintz, V. L. Deringer, A. L. Tchougréeff and R. Dronskowski, J. Comput. Chem., 2016, **37**, 1030–1035.

40 E. G. Hohenstein and C. D. Sherrill, Wiley Interdiscip. Rev. Comput. Mol. Sci., 2012, **2**, 304–326.
41 E. G. Hohenstein and C. D. Sherrill, J. Chem. Phys., 2010, **133**, 14101.
42 T. M. Parker, L. A. Burns, R. M. Parrish, A. G. Ryno and C. D. Sherrill, J. Chem. Phys., 2014, **140**, 94106.
43 R. M. Parrish, L. A. Burns, D. G. A. Smith, A. C. Simmonett, A. E. DePrince, E. G. Hohenstein, U. Bozkaya, A. Y. Sokolov, R. Di Remigio, R. M. Richard, J. F. Gonthier, A. M. James, H. R. McAlexander, A. Kumar, M. Saitow, X. Wang, B. P. Pritchard, P. Verma, H. F. Schaefer, K. Patkowski, R. A. King, E. F. Valeev, F. A. Evangelista, J. M. Turney, T. D. Crawford and C. D. Sherrill, J. Chem. Theory Comput., 2017, **13**, 3185–3197.
44 I. Lončarić, J. Popović, V. Despoja, S. Burazer, I. Grgičević, D. Popović and Ž. Skoko, Cryst. Growth Des., 2017, **17**, 4445–4453.
45 M. K. Panda, T. Runčevski, S. Chandra Sahoo, A. A. Belik, N. K. Nath, R. E. Dinnebier and P. Naumov, Nat. Commun., 2014, **5**, 4811.
46 M. K. Panda, R. Centore, M. Causà, A. Tuzi, F. Borbone and P. Naumov, Sci. Rep., 2016, **6**, 29610.
47 J. M. Sanders, J. Phys. Chem. A, 2010, **114**, 9205–9211.
48 V. L. Deringer, U. Englert and R. Dronskowski, Chem. Commun., 2014, **50**, 11547–11549.
49 S. A. Moggach, W. G. Marshall, D. M. Rogers and S. Parsons, CrystEngComm, 2015, **17**, 5315–5328.
50 K. White and C. Eckhardt, J. Chem. Phys., 1998, **109**, 208-213.
51 J. Nyman and G. M. Day, CrystEngComm, 2015, **17**, 5154–5165.
52 A. P. Chupakhin, A. A. Sidel'nikov and V. V. Boldyrev, React. Solids, 1987, **3**, 1–19.

